ACS APPLIED MATERIALS & INTERFACES

www.acsami.org Research Article

Ultrabroadband Optical Properties of 2D Titanium Carbide MXene

Sean L. Murray,[#] Sahand Serajian,[#] Syed Ibrahim Gnani Peer Mohamed, Shiseido Robinson, Rajavel Krishnamoorthy, Suprem R. Das, Mona Bavarian,[*] Siamak Nejati, Ufuk Kilic,[*] Mathias Schubert, and Mohammad Ghashami[*]

Cite This: *ACS Appl. Mater. Interfaces* 2024, 16, 70763−70773 Read Online

ACCESS | Metrics & More | Article Recommendations | Supporting Information

ABSTRACT: MXenes have rapidly ascended as a prominent class of two-dimensional (2D) materials, renowned for their distinctive optical and electrical properties. Despite extensive exploration of MXenes' optical properties, existing studies predominantly focus on the near-infrared (NIR) to the ultraviolet spectral range, leaving the mid-infrared (mid-IR) range relatively uncharted. In this study, we conducted a comprehensive characterization of the intrinsic optical properties of $Ti_3C_2T_x$ MXene across an ultrabroadband spectral range, spanning from mid-IR (28 meV) to vacuum ultraviolet (VUV, 6.4 eV). For this purpose, $Ti_3C_2T_x$ MXene films of varying thicknesses were coated on quartz substrates, resulting in two distinct categories: thin film samples with thicknesses below 50 nm and bulk-like samples with thicknesses exceeding 500 nm. Using spectroscopic ellipsometry, we analyzed the optical properties of films of various thicknesses and extracted detailed information on their dielectric functions. Our findings reveal resonances in the mid-IR to VUV range. Employing the Lorentz−Drude model to examine these resonances has uncovered the optical resistivity of MXene films and led to the identification of multiple plasmonic modes active in the visible to NIR range, as well as broad band-to-band transition-like resonances in the mid-IR range. This ultrabroadband optical versatility of $Ti_3C_2T_x$ MXene is anticipated to bring about a wide range of thermal and optical applications.

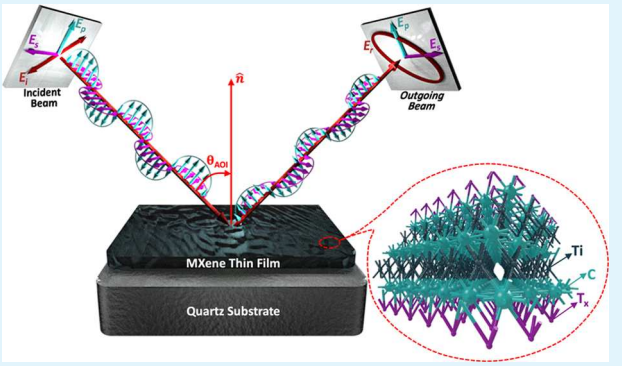

KEYWORDS: *titanium carbide MXene, complex dielectric function, optical properties, IR-active resonances, spectroscopic ellipsometry, thermal and optical applications*

INTRODUCTION

MXenes, an expanding class of two-dimensional (2D) materials comprising transition metal carbides, nitrides, or carbonitrides, have garnered significant attention in recent years.[1−5] These materials are denoted by the generic formula $M_{n+1}X_nT_x$, where M represents a transition metal, X can be carbon or nitrogen, n signifies the number of X atomic layers, and T_x denotes surface terminations such as −F, =O, or −OH.[6−9] Since the discovery of $Ti_3C_2T_x$ as the prototypical MXene, it has been the subject of extensive investigation, revealing exceptional electrical and thermal conductivities,[10−18] and a range of tunable optical properties, including emissivity,[19−21] controllable bandgap,[22,23] and surface plasmon (SP) resonances.[9,11,24,25] The exploration of the tunable SP resonance of $Ti_3C_2T_x$ MXene across a wide spectral range (from 2 to 6 μm) has highlighted its potential in manipulating the optical response within the mid-IR spectrum.[26] The presence of free-carrier plasma oscillations in the NIR spectrum has revealed a critical dielectric to metallic transition at a controversial wavelength within 1100 nm[27] to 1415 nm spectral window for MXene films of varying thicknesses, adding a layer of intrigue and potential for further exploration.[24,27,28] Such groundbreaking attributes have catalyzed the advancement of MXenes in photonics,[29−32] photothermal conversion,[33−35] and thermal management.[36−38] The tunability of SPs has made MXenes valuable for surface-enhanced Raman spectroscopy (SERS),[39] where thicker $Ti_3C_2T_x$ MXene films exhibit enhanced charge transfer effects and absorption in the NIR. Integrating MXenes with silver nanoparticles presented enhanced photothermal conversion efficiencies and extended their applications into wearable heaters, heat barriers, and photothermal therapy.[40] Additionally, MXenes have showcased exceptional capabilities in thermal camouflage, suitable for reducing radiation temperature through low mid-IR emissivity—attributes that contribute to multifunctionality, including discrete Joule heating and

Received: July 22, 2024
Revised: October 7, 2024
Accepted: October 8, 2024
Published: October 22, 2024

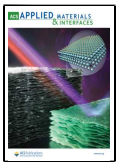

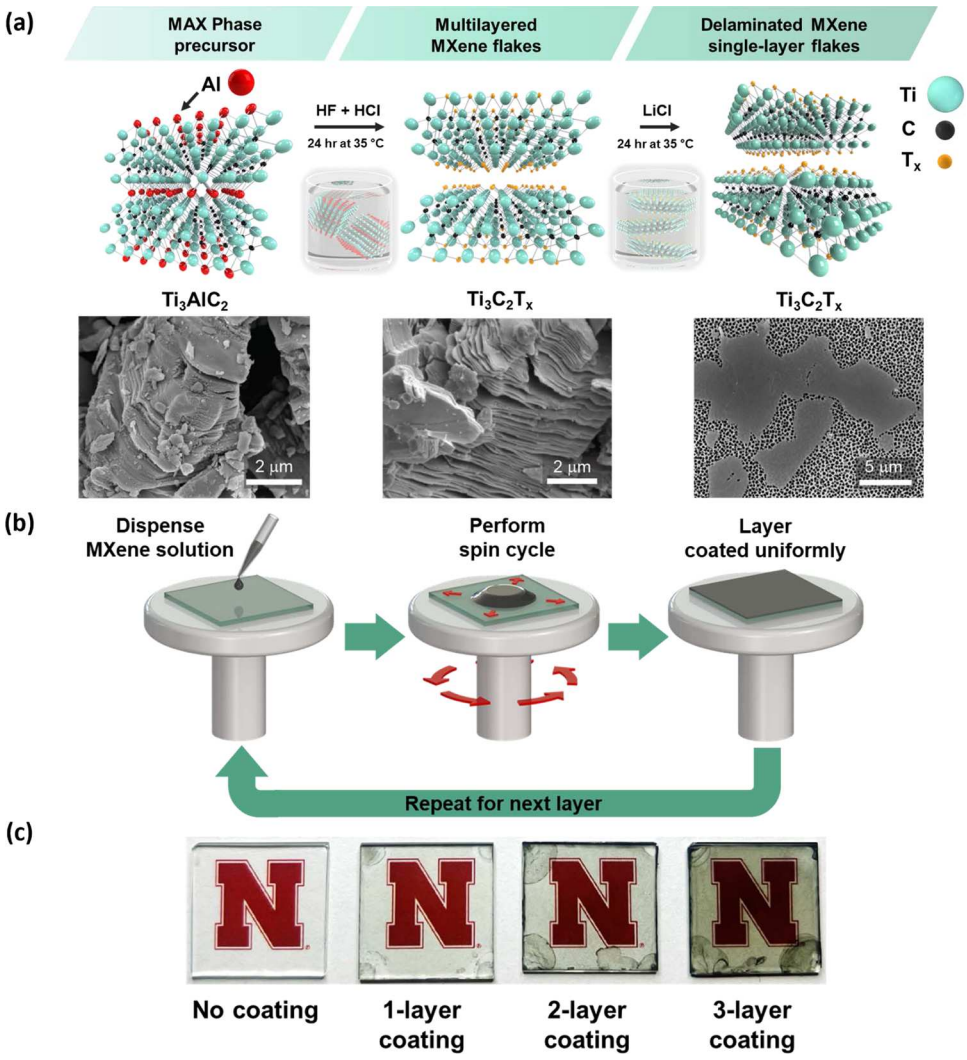

Figure 1. (a) Schematic of $Ti_3C_2T_x$ MXene preparation from the MAX phase precursor via selective etching using the HF-HCl method, resulting in multilayered $Ti_3C_2T_x$ flakes. Subsequent delamination of multilayered flakes into single-layer flakes was achieved using LiCl. Underneath each synthesis step, a corresponding SEM image is shown for more detail. (b) Schematic of the layer-by-layer spin coating deposition of $Ti_3C_2T_x$ for fabricating thin films with varying thicknesses. (c) From left to right: an uncoated quartz sample compared to the fabricated thin films with increasing thickness via successive spin-coating cycles.

superior electromagnetic interference shielding efficiency.[37,41,42]

Amidst the exploration of 2D Titanium Carbide MXene in diverse novel applications, the optical characteristics of this material have been a focal point of research. Yet, experimental characterizations have largely been confined to the NIR to visible range (≈0.4 eV to ≈4 eV). This narrow focus has impeded a holistic understanding of the material's potential and diverse optical behaviors. Furthermore, the correlation of previously reported optical properties with thin film thickness—directly influenced by fabrication parameters—presents an additional layer of complexity. The variability in the dielectric function reports underscores the challenge of discerning the material's optical characteristics, independent from the nuances of its production.[24,27,43,44]

Herein, we report the ultrabroadband optical properties of $Ti_3C_2T_x$ MXene thin films, prepared with thicknesses ranging from 13 to 876 nm. The optical properties of these stacked films are studied using spectroscopic ellipsometry (SE) across an expanded spectral range from 28 meV to 6.4 eV. Our methodology incorporates a multisample analysis (MSA) technique to determine the film thickness and the frequency-dependent dielectric function simultaneously. Our findings not only affirm the consistency of the wavelength-by-wavelength complex dielectric function of $Ti_3C_2T_x$ MXene thin films and bulk-like sets with previously documented research but also uncover additional resonances not yet explored experimentally. This discovery broadens our understanding of the optical response of $Ti_3C_2T_x$ MXene, marking a significant advancement in the study of this novel family of 2D materials and its potential applications, especially in thermal radiation and nanoscale thermal control. Furthermore, our observation of the dielectric-metal duality in MXene films within the near-IR range underscores their versatile functionality, offering tunable characteristics to reach high electrical conductivity, extreme thermal properties, tunable dielectric constants, and exceptional mechanical flexibility. Such versatility opens up a broad array of possibilities for applications, ranging from energy storage and conversion to sensors and flexible electronics, where precise control over electrical and optical properties is essential.

https://doi.org/10.1021/acsami.4c12079
ACS Appl. Mater. Interfaces 2024, 16, 70763−70773

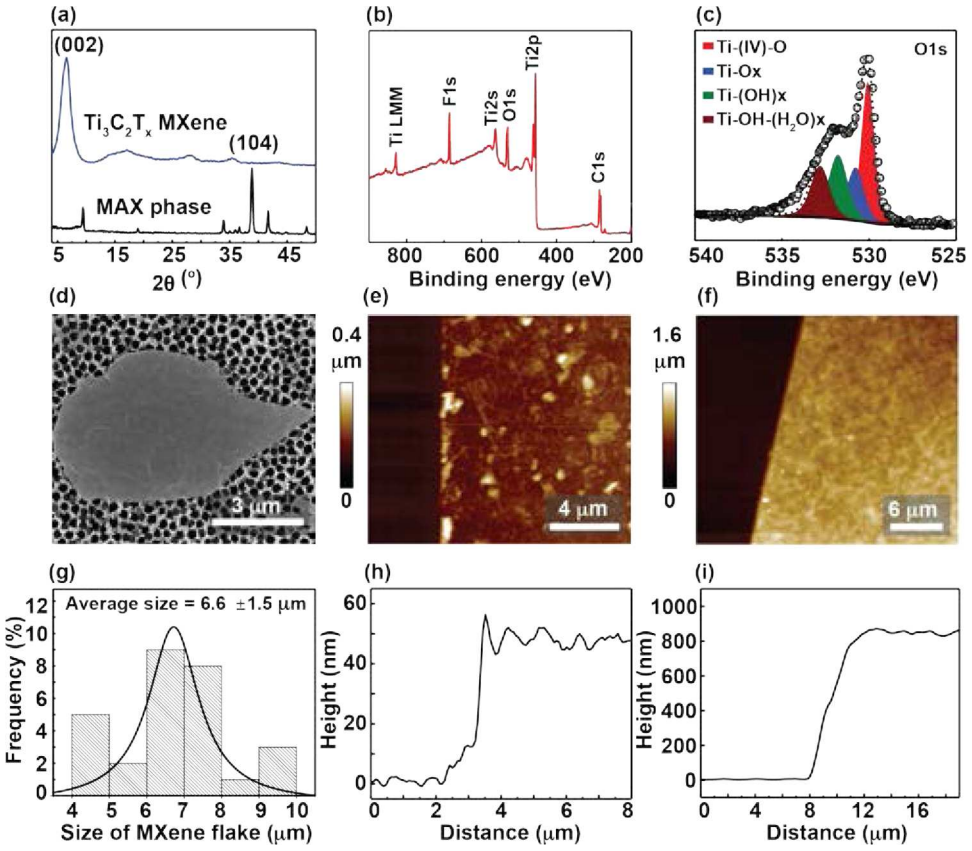

Figure 2. (a) PXRD spectrum of MAX phase and $Ti_3C_2T_x$ MXene. (b) XPS survey and (c) O 1s high-resolution spectra of $Ti_3C_2T_x$ MXene. (d) SEM image of a single $Ti_3C_2T_x$ MXene flake on AAO disk and (g) flake size distribution. (e) and (f) AFM height image of MXene with different thicknesses coated on quartz. (h) and (i) show the height profile of the corresponding film.

RESULTS AND DISCUSSION

$Ti_3C_2T_x$ MXene Characterization. $Ti_3C_2T_x$ MXene used in this study was synthesized by selectively etching aluminum from its MAX phase using HF and HCl, producing a dispersion of multilayer $Ti_3C_2T_x$ MXene flakes. To achieve single-layer flakes, the multilayer flakes were delaminated using LiCl (see Figure 1(a)). This dispersion was then used for spin coating, with the flakes characterized for their chemical and structural properties.

Figure 2(a) illustrates the PXRD patterns of Ti_3AlC_2 MAX powder and $Ti_3C_2T_x$ MXene. The shift of the (002) peak toward a lower 2Θ angle and the absence of the strong peak at 39° suggest the transformation from Ti_3AlC_2 into $Ti_3C_2T_x$ MXene. Figure 2(b) shows the XPS survey spectrum of $Ti_3C_2T_x$ MXene, confirming the presence of all its constituent elements. Additionally, the high-resolution O 1s spectrum was deconvoluted into four distinct peaks, as reported previously.[45] As displayed in Figure 2(c), the peaks centered at 529.7, 531.1, 532.5, and 533.8 eV were assigned to Ti−(IV)−O, Ti−O_x, Ti−$(OH)_x$, and Ti−OH−$(H_2O)_x$ species, respectively. Based on this spectrum, the atomic percentage of −OH terminations on the titanium surface was determined to be 16.9%. The Ti2p peak (Figure S1) was further analyzed to calculate the atomic percentages of −O and −F terminations on the titanium surface to be 18.1 and 21.0%, respectively.

Figure 2(d) presents an SEM image clearly showing the straight edges of $Ti_3C_2T_x$ MXene single flakes. The size distribution of these flakes in the as-prepared dispersion, measured from SEM images, is shown in Figure 2(g), with an average flake size of 6.6 ± 1.5 μm. The dispersion containing single-layer $Ti_3C_2T_x$ MXene flakes was employed to fabricate both thin films and bulk-like films, which were then deposited onto quartz substrates, as depicted in Figure 1(c). The representative AFM height images of the MXene thin films are shown in Figures 2(e),(f), while Figure 2(h),(i) showcase the height profile images of these films. Additional AFM images detailing various thicknesses of MXene coated on quartz are also provided in Figures S2 and S3. Surface roughness measurements derived from the AFM data are compiled in Table 1, indicating an increase in roughness with the number of spin-coated layers. Specifically, the average roughness for the bulk-like film set (38.3 nm) was found to be approximately four times larger compared to the thin film set (9.3 nm). It is noteworthy that the roughness measurements taken near scratches—created for thickness extraction—may exaggerate the roughness and thickness values, which were observed to be

Table 1. Surface Roughness Measurements of MXene Films with Various Thicknesses Coated on Quartz

film type	sample #	thickness (nm)	roughness (nm)
thin film	1	13 ± 2.0	7 ± 0.2
	2	20 ± 1.5	8 ± 0.7
	3	43 ± 2.1	13 ± 0.5
bulk-like	1	776 ± 5.0	41 ± 2.4
	2	820 ± 3.0	39 ± 1.1
	3	876 ± 4.5	35 ± 0.8

https://doi.org/10.1021/acsami.4c12079
ACS Appl. Mater. Interfaces 2024, 16, 70763−70773

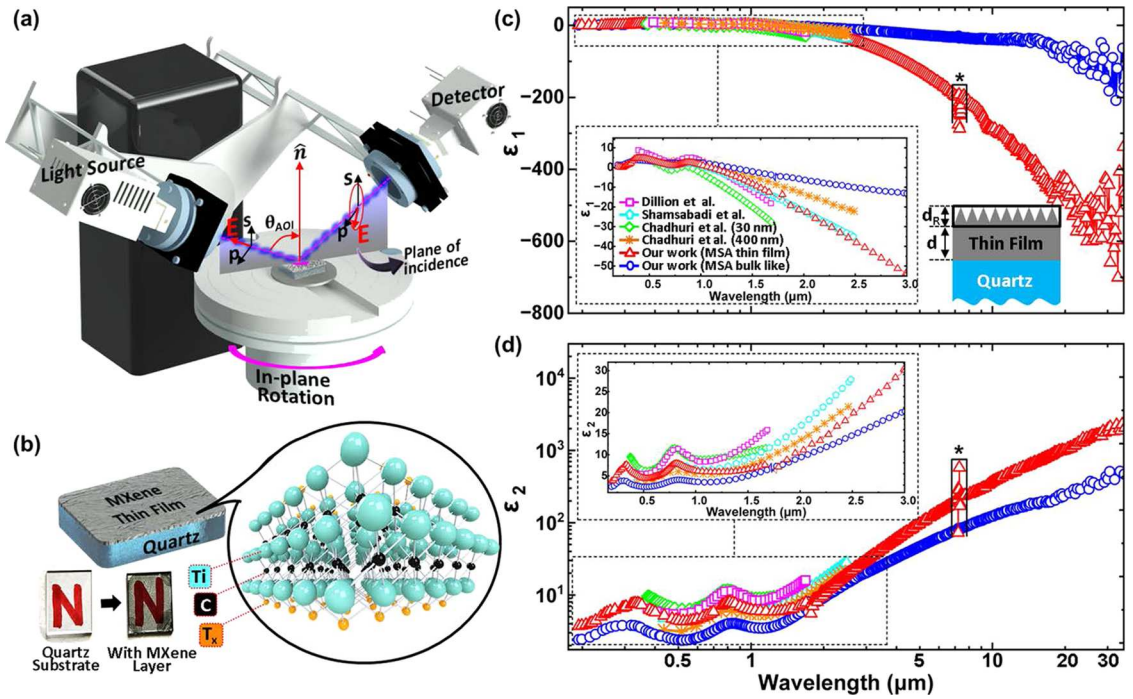

Figure 3. (a) Schematic illustration of spectroscopic ellipsometry instrument (note: the schematic shows RC2 J.A. Woollam ellipsometer instrument that operates within NIR to VUV spectral range) and its working principle. The change in the polarization state of light due to its interaction with the sample under investigation is detected and recorded in terms of (Ψ, Δ), as shown in Supporting Information Figure S4 for MXene samples, and Figure 6 for the quartz substrate. (b) MXene thin film from 2D MXene flakes on quartz substrate and zoom-in schematic view of the molecular configuration of MXene flake. Wavelength-by-wavelength determined dielectric constants of the two different sets of MXene thin films extracted using the MSA approach. The complex dielectric function (real and imaginary parts are shown in (c) and (d), respectively) depicted with blue star symbols are obtained from MSA analysis based on the thin films with thicknesses ranging from ≈5 nm to ≈30 nm, the dielectric function depicted with the red pentagon symbols are obtained from MSA analysis based on the thin films with thicknesses ranging from ≈450 nm to ≈950 nm. The dielectric function spectra of MXene thin films from the literature were also inlaid with our findings for comparison. Insets in (c) and (d) are zoom-in plots to the NIR-VUV spectral range. The feature highlighted by the black star symbol in both real and imaginary parts of the dielectric function is an artifact that in this spectral range, the substrate has vanishing reflectance and hence the error bars on the measured Ψ and Δ values are very large in this narrow spectral range. The error bars are on average approximately ±2% and are much smaller than the symbol sizes used to differentiate the various curves in (c) and (d). Numerical values and error bars from regression analysis are given in the Supporting Information.

much lower from the data obtained via the multisample analysis.

Optical Response of 2D MXene Films. The linear (absorption, transmission, and photoluminescence) and nonlinear (saturated absorption and nonlinear refractive index) optical properties of MXene material are fundamentally connected to its unique energy band structure.[1,5] This structure encompasses critical aspects such as the band gap, the nature of the bandgap (direct or indirect), other critical points, and topological characteristics. Central to these properties is MXene's dispersion behavior and its nonlinear complex dielectric function (ε).

The multisample analysis (MSA) of the spectroscopic ellipsometry (SE) data provided the calculated real (ε_1) and imaginary (ε_2) components of the complex dielectric function for MXene thin films, as depicted in Figure 3(c),(d). These findings are compared with previously reported data, which covered a limited spectral range.[24,27,44] The discrepancies between the previously reported dielectric functions and those found in our study are largely attributed to variations in synthesis method and deposition parameters, such as dispersion concentration and spin-coating specifics. Moreover, our results demonstrate a considerable variation in the dielectric function depending on film thickness. In the case of the bulk-like set, an increase in the dielectric function is evident, especially in the mid-IR range where metal-like behavior predominates. This trend is shown in Figure 3(c),(d), where the dielectric functions obtained from the MSA are represented by red triangles for the thin film sample set (ranging in thickness from 5 to 30 nm), and by blue circles for the bulk-like sample set (ranging in thickness from 450 to 950 nm). This pattern aligns with observations by Chaudhuri et al., who also reported similar increases in the dielectric function within a narrower spectral range, depicted by green diamonds (30 nm) and orange stars (450 nm) in Figure 3(c),(d).[24] The dielectric function of MXenes is known to be influenced by factors such as composition (e.g., Ti_3C_2, Nb_2C, V_2CT_x), synthesis conditions (e.g., etching methods, precursor materials), and deposition parameters (e.g., film thickness, substrate interaction). Each of these factors can result in variation's in the dielectric response, which might alter dielectric and optoelectronic properties.[27,46] The transmission measurements for both thin film and bulk-like film sets is reported in Figure S5.

The SE data-based MSA approach also provides measurements of thin film thickness and surface roughness, which are summarized in the Supporting Information Table S4. We observe notable differences between the measurements obtained through AFM imaging and the SE-based approach. The roughness values derived from SE analysis were

https://doi.org/10.1021/acsami.4c12079
ACS Appl. Mater. Interfaces 2024, 16, 70763−70773

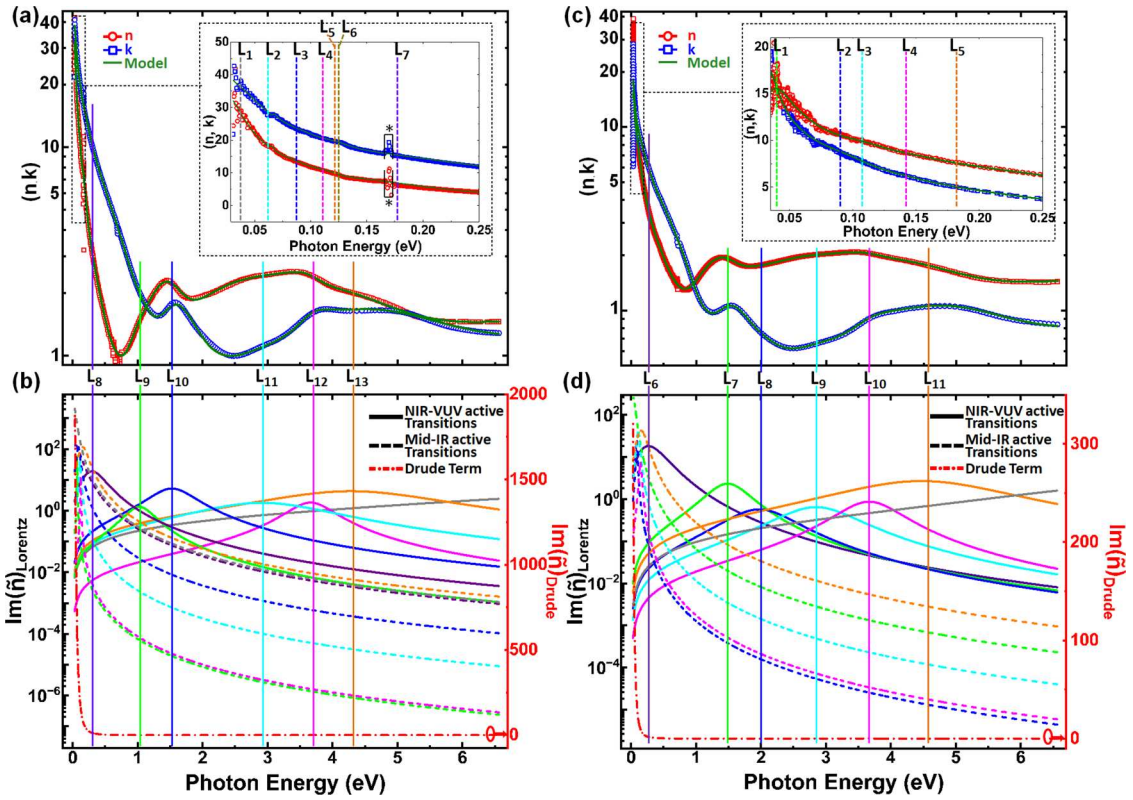

Figure 4. Unraveling VUV to NIR band-to-band transitions and mid-IR active resonance modes of MXene thin films from SE data based CPMDF analysis. (a and c) Spectral evolution of complex refractive index ($\tilde{n} = n - ik$) obtained from multisample analysis based on wavelength-by-wavelength SE data analysis. The blue and red symbols correspond to the refractive index and extinction coefficient spectra, respectively. The wavelength-by-wavelength analysis result (symbols) is overlaid with the generated physical line shapes (green solid lines) of the complex refractive index from CP analysis. The inset focuses on the mid-IR section of the spectrum and highlights the central energy of CP functions with vertical dashed lines in the same color codes utilized in part-b. (b and d) The amplitude of imaginary part of spectral evolution of individual oscillator function (Lorentz (left axis black color) and Drude (right axis, red color) functions) is utilized in the proposed DL model of CPMDF analysis. The red dashed-dot line shows the Drude contribution in the DL model. While the dashed lines correspond to the Lorentz oscillators active in the mid-IR part of the spectra, the solid lines correspond to the Lorentz oscillators active in NIR to VUV. While (a) and (b) are obtained from the thin film set with thicknesses ranging from ≈5 nm to ≈30 nm, (c) and (d) correspond to the analysis of bulk-like set with thicknesses ranging from ≈450 nm to ≈950 nm.

significantly lower than those measured via AFM. This discrepancy likely stems from the simplified roughness model used in the SE analysis, which treats roughness as an effective medium of voids and material. Such simplification may not fully capture the complexities the spin-coating process introduces, including potential nonuniformities, pinholes, and spikes. On the other hand, the scratch-based thickness measurements from AFM might artificially inflate the structural parameters due to local strain and stress effects on the thin film, potentially leading to overestimated values (refer to Table 1 for the values obtained from AFM analysis).

Building on the findings from our MSA based on SE data, which detailed the extraction of the complex dielectric function spectra via wavelength-by-wavelength regression shown in Figures 3(c),(d), we now focus on identifying and modeling CP contributions to the MXene dielectric function. This involves the integration of a Drude term with multiple Lorentzian broadened oscillators. This modeling strategy enabled us to characterize the dielectric function's physical line shapes across an unprecedentedly broad spectral range—from 194 nm to 35 μm—for MXene thin films, which is the broadest range reported to date for these materials, to the best of our knowledge. Our analysis, utilizing two distinct sample sets varying in thickness, highlights the pivotal role of thin film thickness in influencing the physical line shapes and amplitudes observed in the extracted complex dielectric function spectra. The thickness of the films significantly affects their optical properties, underscoring the importance of precise film fabrication and characterization in understanding and leveraging the unique attributes of MXenes.

In order to clearly illustrate the contribution of each resonance and the identification of CPs for both sample sets, we presented the refractive index and extinction coefficient spectra separately for each set (see Figures 4(a) and (c)). Strikingly, the optical constants determined through wavelength-by-wavelength analysis and MDF analysis are virtually indistinguishable, indicating an excellent fit of the model. Specifically, Figure 4(a) displays the refractive index and extinction coefficient spectra for the thin film set while Figure 4(c) showcases the same for the bulk-like set. By taking advantage of the SE data-based CP-MDF analysis, we have successfully identified the individual contributions of each CP and the direct band-to-band transitions. These contributions to the overall dielectric function are further elucidated in Figures 4(b) and (d) for both sets. Additionally, the parameters defining each oscillator—central energy, amplitude, and broadening—are systematically cataloged in Supporting Information Tables S2 and S3.

https://doi.org/10.1021/acsami.4c12079
ACS Appl. Mater. Interfaces 2024, 16, 70763−70773

To more accurately represent the MXene's optical properties, particularly within the mid-IR spectrum, our model incorporates additional Lorentz oscillators beyond the conventional Drude model. This extension is crucial to adequately represent the observed non-Drude behavior. Notably, our analysis of the thin film set identified four distinct mid-IR resonances alongside three additional broad shoulders, indicating significant optical activity in these regions. These resonances characterized by their central peaks are provided in the Supporting Information Tables S1 and S2, and are visually detailed in Figure 4(b) as dashed lines.

Contrasting with the thin film set, we employed five Lorentz oscillators for the bulk-like set to characterize mid-IR resonance features. These features identified by their central peaks, along with an additional broad shoulder, are provided in the Supporting Information Tabels S1 and S2, and illustrated in Figure 4(d) with dashed lines. Using the Drude function parameters, we can optically extract further information from the CP-MDF analysis on the electronic properties of the MXene thin films. The specific Drude model parameters are detailed in Supporting Information Table S4. Notably, the bulk-like set exhibited a higher resistivity value of 29.37×10^{-5} Ω·cm, compared to the thin film set at 2.91×10^{-5} Ω·cm. This increase can be attributed to the colloidal deposition process of MXene, which likely promotes the formation of oxide components more extensively than in the thinner films.

Overall, within the CP-MDF analysis, the representation of optical behaviors differs between the MXene thin film and bulk-like sets. For the thin film set, 14 Lorentz oscillators are necessary to capture both NIR-VUV inter- and intra- band-to-band transitions and mid-IR active resonances. In contrast, only 12 Lorentz oscillators are sufficient to describe the dielectric function of the MXene bulk-like set. Specifically, seven Lorentz oscillators are consistently dedicated to capturing the nuances in the higher energy domain (VUV-NIR). However, the distinction arises in the mid-IR region: the thin film set requires seven additional oscillators for this purpose, whereas the bulk-like set uses only five to effectively model the mid-IR active resonance modes. The insets in Figure 4(a),(c) focus on the mid-IR section of the spectrum, highlighting the central energy of CP functions with vertical dashed lines in the same color codes utilized in Figure 4(b),(d) (dashed lines). To address concerns about overfitting, tables with the numerical uncertainty limits within the 90% confidence interval and values of the correlation matrix for all parameters are included in the Supporting Information. We find small error bars and small correlations only between all model parameters. This agrees also with the observation that all features introduced by the Lorentz oscillators included here correspond to features observable in the experimental data, as indicated in Figure 4.

Importantly, we identify two broad resonance modes within the VIS-NIR spectral range: (i) spanning from 200 to 500 nm and (ii) from 600 to 1100 nm, as illustrated in Figure 4. Notably, the real part of the dielectric function remains greater than zero for both MXene sets (thin film and bulk-like), suggesting that under the influence of an electric field, charges within the material may shift, resulting in the formation of an induced dipole moment. This phenomenon signifies the collective oscillation of free electrons, indicative of plasmonic mode characteristics. However, to accurately capture the physical line shapes of these observed peaks in the wavelength-by-wavelength approach and determine the complex dielectric function, we employed multiple Lorentz oscillators in the CP-MDF analysis. This complexity suggests that these emerging peaks may not purely represent plasmonic resonances. To associate features observed in the complex dielectric function with specific electronic properties of a given MXene sample requires DFT calculations.[47] Based on DFT calculations reported in the literature, these absorbance peaks may stem from van Hove singularities or nonsingular peaks in the joint density of states, with several inter- and intraband transitions prevalent within these spectral ranges.[24,28,48]

Furthermore, we observe a transition from dielectric to metallic behavior at approximately 1.01 and 1.35 μm for the thin film set and bulk-like set, respectively. This transition is indicative of the resonant coupling between the electromagnetic field and the collective oscillation of free electrons, characteristic of surface plasmon polaritons at the MXene interface in the near- and mid-infrared ranges.[24,48,49] In essence, MXene thin films exhibit a dual dielectric and plasmonic or metallic response, positioning them as promising materials for next-generation photonic and optoelectronic devices,[50,51] quantum systems,[52] and cancer theragnostic applications.[53] At longer wavelengths, the dielectric function's real part becomes highly negative upon transitioning from dielectric to metal, indicating stronger metallic behavior compared to typical metals. This property could be utilized to regulate electromagnetic field magnitudes incident on surfaces coated with thin MXene films, potentially enabling the manipulation of thermal radiative transfer.

The observed differences in the extinction coefficient (refer to Figure 3) and optical resistivity (detailed in Table S3) between these MXenes film sets (i.e., bulk-like set and thin film set) can also be attributed to the residual water content and the depletion of hydroxyl groups within the film structure. Moreover, the presence of different termination groups of the micro flakes within the spin-coated films may further influence the optoelectronic properties.[44]

These findings not only enhance our understanding of MXene's optical properties but also suggest promising applications across several technological areas. The observed transition from dielectric to metallic behavior in the near-IR range could be leveraged for tunable plasmonic devices, particularly for sensing and spectroscopy. The high conductivity and tunable optical response in the mid-IR range indicate the potential for advanced thermal management solutions, such as smart windows or energy-efficient building materials. Additionally, the strong absorption and tunability in the NIR range make these films ideal candidates for photothermal conversion applications, including wearable heaters and photothermal therapies. To verify these applications, future studies should focus on in situ emissivity and reflectivity measurements, especially at elevated temperatures, to assess their performance in thermal management and photothermal systems. Although challenges such as long-term stability and optimizing integration with other materials remain, the unique optical properties and versatility of $Ti_3C_2T_x$ MXene make it a promising candidate for next-generation optical, thermal, and optoelectronic applications.

CONCLUSIONS

In summary, SE measurements were performed to study the optical properties of $Ti_3C_2T_x$ MXene films. These thin and bulk-like films were fabricated on quartz substrates using a layer-by-layer spin-coating method. Through a multisample

https://doi.org/10.1021/acsami.4c12079
ACS Appl. Mater. Interfaces 2024, 16, 70763−70773

analysis (MSA) approach, we simultaneously extracted these films' thickness and complex-valued dielectric function. Our analysis demonstrated a high degree of consistency with previously reported data. Importantly, our measurements encompassed a broad spectrum ranging from mid-IR (28 meV) up to VUV (6.4 eV), unveiling 13 previously unidentified resonances: six in the VUV-NIR range and seven in the mid-IR range. These newly discovered resonances possess the potential to elucidate novel underlying mechanisms, as they offer the capability to manipulate plasmonic resonances. Notably, the observed transition from dielectric to metallic behavior implies the presence of surface plasmon polaritons at the MXene-air interface. This distinctive plasmonic response opens up exciting opportunities for various radiative applications, including electromagnetic interference shielding, localized thermal management, and thermal insulation. Ultimately, this work underscores the versatile optical response of $Ti_3C_2T_x$ MXene, highlighting its potential to reveal new physical mechanisms and enhance technological applications.

MATERIALS AND METHODS

$Ti_3C_2T_x$ MXene Synthesis and Characterization. The synthesis and delamination of single-layer MXene flakes were conducted through a two-step process. First, Ti_3AlC_2 MAX phase powder (Titanium aluminum carbide 312, ⩾90% purity, ≤40 μm particle size, Sigma-Aldrich) was chemically etched using a solution composed of 6 mL deionized (DI) water, 12 mL Hydrochloric Acid (12M, ACS grade, Fisher Science Education), and 2 mL Hydrofluoric Acid (48%, ACS reagent, Sigma-Aldrich). To initiate etching, 1 g of Ti_3AlC_2 MAX phase powder was gradually introduced to the solution over 15 min to dissolve the aluminum layers. The mixture was continuously stirred for 24 h at a constant temperature of 35 °C using a silicon oil bath. Poststirring, the MXene product was separated using centrifugation at 3600 rpm for 5 min and then washed multiple times with DI water to attain a pH of approximately 6.0. During the delamination phase, 1 g of anhydrous Lithium Chloride (99% purity, Alfa Aesar) was added to the mixture, which was then stirred at 35 °C for an additional 24 h (see Figure 1(a)). To achieve a target concentration of approximately 5 mg/mL, the MXene dispersion was freeze-dried at 35 °C using a Thermo Fisher Savant SpeedVac Concentrator (Model SPD111 V) along with a Savant RVT4104 Refrigerated Vapor Trap from Thermo Scientific. This process yielded a dispersion of single-layer MXene flakes in DI water.

The synthesis of $Ti_3C_2T_x$ MXene bulk-like film was made by etching aluminum-rich Ti_3AlC_2 MAX phase material (Y-Carbon, Ltd.) using a mixture of LiF and HCl in a ratio of 12 M LiF to 9 M HCL. The mixing was made by stirring the materials for 10 min at a temperature of 45 °C at 200 rpm using a magnetic stirrer (henceforward the mixture is termed as "etchant"). Subsequently, 1 g of the above MAX powder was gradually added to the etchant while the whole material was undergoing continuous stirring (at 200 rpm and 45 °C) for 48 h. These parameters thus used were the optimal parameters for aluminum interlayer removal and separation from the MAX phase to produce the aggregated MXene layers. The acidic material, including any trace amount of the same, was removed by washing the product multiple times with DI water using a centrifuge (Hermle Labortechnik GmbH, model Z 36 HK). Each washing cycle was for 5 min conducted at 3500 rpm and a vortex was used in between each washing cycle to delaminate the aggregated MXene layers. The process was followed until the pH value of the supernatant reached between 6.0 to 7.0. The final exfoliation process was conducted by transferring the solution to a centrifuge tube conducting a final vortex, and then centrifugation at 3500 rpm for 15 min. The supernatant from this final centrifuge process was discarded to avoid any presence of the unetched material as well as thicker MXene. The obtained MXene clay was added to an appropriate amount of DI and vortexed for 15 min to have the final material for the spin coating.

The quartz slides used as the substrate for MXene thin film deposition are GE-124 fused quartz with an electrical resistivity of 7×10^7 ohm-cm at 350 °C from Chemglass Incorporation. Before the spin-coating of MXene dispersion, a thorough cleaning protocol was implemented to prepare the quartz substrates, each measuring 2 × 2 cm^2. Initially, the substrates were immersed in boiling chloroform to remove any organic contaminants. This was followed by a 10 min ultrasonic bath in ethanol, further purging the surfaces. The cleaning sequence concluded with a 15 min exposure to UV Ozone treatment using a Novascan Pro Series Digital UV Ozone System, followed by a 30 min incubation period. These procedures were specifically designed to augment the surface energy and wettability of the quartz substrates, thus promoting superior adhesion for the subsequent thin film coatings.

To coat single-layer MXene as thin films with varying thicknesses, MXene flake dispersion was employed. Utilizing a Laurell Spin Coater (Model WS-650MZ-23NPB), the films were deposited on precleaned quartz substrates through a layer-by-layer spin-coating technique. As illustrated in Figure 1(b), each layer began with the application of 0.2 mL of the dispersion to the center of a substrate, followed by a two-step spinning process—initially at 500 rpm for 30 s, then at 1700 rpm for 20 s. Additional layers were applied immediately following the deposition of the previous layer to achieve films of desired thicknesses. To create thicker MXene films, the spin coating of the MXene clay dispersion was done on 4 mm × 4 mm quartz substrates. To control film thickness, three different spin speeds of 750, 1000, and 1500 rpm were used; first, the dispersion spun at 500 rpm for 10 s, followed by spinning at the target speed. After the uniform films were made, they were dried in a vacuum sample storage overnight.

Characterization of the MAX phase and MXene materials commenced with Powder X-ray diffraction (PXRD) analysis, employing a Rigaku SmartLab instrument outfitted with Cu Kα radiation. For this analysis, MXene film was prepared by vacuum filtration, utilizing nylon media with a nominal pore size of 200 nm. The resultant MXene thin film was detached from the substrate, cut into 2 cm × 2 cm pieces, and securely attached to a glass plate using double-sided tape. The PXRD patterns were collected under Bragg–Brentano geometry at a scan rate of 5° per minute, facilitating the determination of crystalline structure and phase purity. Surface elemental composition and bonding configurations within the MXene were elucidated through X-ray photoelectron spectroscopy (XPS) using a ThermoFisher α instrument. Survey spectra were obtained with a 400 μm spot size, a 100 ms dwell time, and a pass energy of 200 eV, while high-resolution spectra were acquired under identical spot size and dwell time but with a reduced pass energy of 50 eV to enhance spectral resolution. The morphology of the MXene flakes was visualized using a FEI Helios NanoLab 660 scanning electron microscope (SEM). Sample preparation involved vacuum drying at room temperature and a brief 10-s platinum sputter coating using a Ted Pella 108 auto system to improve electron conductivity. The prepared samples were mounted on carbon conductive tape on SEM stubs. Imaging was performed with a 10 keV electron beam and a working distance of 4 μm, providing high-resolution insights into the flake's surface features.

Ellipsometry Measurements and Analysis. To cover a comprehensive spectral range from 28 meV to 6.4 eV, the Spectroscopic ellipsometry (SE) data were gathered using two distinct instruments. For the UV–vis-NIR segment, we employed the *J. A. Woollam Co. RC2* dual rotating compensator SE instrument, conducting measurements across seven angles of incidence (θ_{aoi}, ranging from 45° to 75° in 5° increments), within a spectral domain of 0.72 to 6.4 eV (193 to 1690 nm). The mid-IR spectrum, extending from 28 meV to 0.72 eV (1.7 to 44 μm), was collected using *J. A. Woollam IR-VASE Mark-II* SE instrument at two specific angles of incidence (θ_{aoi}), 50° and 70°. All experimental procedures were executed at room temperature under standard ambient conditions.

The core of the ellipsometry technique involves measuring the complex reflectance ratio (ρ) at various frequencies, represented by

https://doi.org/10.1021/acsami.4c12079
ACS Appl. Mater. Interfaces 2024, 16, 70763–70773

the equation $\rho = \frac{r_p}{r_s} = \tan(\psi)e^{i\Delta}$. Here, r_p and r_s denote the complex Fresnel reflection coefficients for *p*-polarized (parallel to the incident plane) and *s*-polarized (perpendicular to the incident plane) light, respectively see Figure 3(a). The parameter ψ characterizes the amplitude ratio change between the two polarizations, while Δ signifies their phase difference. Given the amorphous nature of the MXene thin films on quartz substrates, to simplify the analysis, SE data were not collected in varying in-plane sample rotations. A rotation-dependent spectral evolution of SE data at $\theta_{aoi} = 65°$, confirming the absence of optical anisotropy with respect to the in-plane orientation of the MXene thin film on the quartz substrate, is provided in the Supporting Information (see Figure S7). SE data were analyzed using the WVASE software package (from *J. A. Woollam Co.*), employing a three-layer model comprising the substrate, thin film, and surface roughness. Hence, the dielectric function of each layer plays a key role in accurately estimating the thickness and roughness of the thin film. By knowing the complex dielectric function of the substrates (as provided in the Supporting Information), this layered model is used to simultaneously determine the spectral complex dielectric function of MXene thin films, thickness, and roughness.

The model's efficacy is derived from iterative best-match calculations, using nonlinear regression algorithms to fine-tune the alignment between theoretical and experimental SE data. These adjustmentable parameters were [involves parameters such as] layer thickness and permittivity values. The quality of fit is quantitatively assessed through the mean square error (MSE), serving as a key indicator of the model's accuracy in replicating the measured data. The fitting process utilizes the Marquardt−Levenberg algorithm, specifically designed to minimize the MSE by adjusting the fit parameters accordingly. Achieving the minimum MSE signifies the attainment of the best-match model, indicating the highest degree of correspondence between the model predictions and experimental observations. Furthermore, this numerical analysis elucidates the correlation and uncertainty of the model parameters, with their confidence delineated within a 90% confidence interval.

Multi-Sample Analysis (MSA). The MSA approach employed in this study is a widely used technique for simultaneously determining the thickness and the complex-valued, frequency-dependent dielectric function of thin films.[54−57] This method uniquely enables the extraction of the dielectric function across various wavelengths without relying on predefined physical model line-shape functions.[58] Additionally, these samples must exhibit significant variations in thickness to facilitate accurate analysis. Within this analytical framework, our model is adept at accommodating more intricate scenarios, including the impacts of surface and interface roughness as well as porosity.[59,60] This is achieved by introducing a roughness layer on top of the thin film layer in the model, which accounts for the optical influence of surface irregularities on the ellipsometric spectra. The optical properties of this hypothetical roughness layer are determined using an effective medium approximation (EMA), which blends the dielectric functions of the material and air in equal proportion.[61] Therefore, this method has proven effective in accurately predicting the mean square roughness of surfaces, especially when the roughness parameters are minimal relative to the wavelength.[62,63] The roughness and thin film thickness values, estimated based on the MSA method, are presented in the Supporting Information (see Table S4).

Critical Point Model Dielectric Function Analysis (CP-MDF). The electronic band-to-band transitions give rise to critical-point (CP) features, observable in the dielectric function spectrum. To analyze these features, a model dielectric function (MDF) framework was utilized, incorporating physically interpretable line-shape functions, with parameters refined through MDF analysis.[64] Our analysis employs the Drude-Lorentz model, which combines a Drude term with several Lorentz oscillators to describe the optical properties of metal species, including their free carrier concentrations and inter- and intraband transitions. The Drude term accounts for the free charge carrier effects and intraband transitions predominantly observed in the mid-IR range. Meanwhile, the interband transitions, which manifest in the UV−vis-NIR spectrum as polaronic or bipolaronic absorption bands, are modeled by incorporating an appropriate number of Lorentz oscillators.[65,66] Hence, combining a Drude term with multiple Lorentz oscillators gives the proposed Drude-Lorentz model approach as follows[67]

$$\tilde{\varepsilon}(E) = \varepsilon_1 + i\varepsilon_2 = \varepsilon_\infty + \left(\frac{-A_D B_D}{E^2 + iB_D E}\right) + \sum_n \frac{A_n B_n E_n}{E_n^2 - E^2 - iB_n E} \quad (1)$$

Here ε_∞ represents the high-frequency limit of the dielectric function, acting as a real-valued offset in the model. The second term in eq 1 represents the Drude contribution, with amplitude A_D and broadening parameter B_D, capturing the free electron contributions. The third term is the generalized mathematical expression of the Lorentz oscillators utilized in the CP-MDF analysis. For the *n*th Lorentz oscillator, A_n is the amplitude, E_n is the center energy, and B_n is the broadening of the oscillator. E is the photon energy in electron-volts and is equal to $h\nu$ where h and ν are the Planck's constant and the frequency, respectively.[68] The real part of the dielectric function, ε_1, is subsequently obtained using Kramers−Kronig relation shown in eq 2[55,69]

$$\varepsilon_1(E) = \frac{2}{\pi}\mathcal{P}\int_0^\infty \frac{\xi\varepsilon_2(\xi)}{\xi^2 - E^2}\,\mathrm{d}\xi \quad (2)$$

where $\mathcal{P}$ denotes the Cauchy principle value of the integral, and ξ is the integration variable. Importantly, the Drude contribution is a basic classical model to describe the electrical conductivity of metals and other conductors.[66,70] Alternatively, the second term in eq 1, can be expressed in terms of the plasma frequency (ω_p) and the momentum-averaged scattering time (τ) by considering the following conversion of amplitude and broadening parameters $A_D = \hbar w_p^2\tau$ and $B_D = \hbar/\tau$, respectively. It is important to state that the classical Drude term describes the free carrier effects on the dielectric response of the sample under investigation and it is in the form of a Lorentz oscillator function with zero center energy (i.e., no restoring force). The Lorentz oscillator employs a heavy mass connected to a light mass with a spring to describe the optical response of the bound state of an electron orbiting around the nucleus that is driven by an oscillating electric field. Hence, the Lorentz−Drude model approach involves modeling an electron as a driven damped harmonic oscillator.

■ ASSOCIATED CONTENT

Data Availability Statement

The data sets generated during and/or analyzed during the current study are available from the corresponding author upon reasonable request.

Supporting Information

The Supporting Information is available free of charge at https://pubs.acs.org/doi/10.1021/acsami.4c12079.

Additional topological measurements; High-resolution XPS Ti2p spectrum; Detailed SE Optical Analysis; Drude-Lorentz oscillator parameters employed in the critical point model dielectric function; Experimental SE Ψ and Δ data; $Ti_3C_2T_x$ MXene film transmission measurements (PDF)

Correlation and all parameter lists (XLSX)

■ AUTHOR INFORMATION

Corresponding Authors

Mona Bavarian − *Chemical and Biomolecular Engineering Department, University of Nebraska-Lincoln, Lincoln, Nebraska 68588, United States;* orcid.org/0000-0001-7689-773X; Email: mona.bavarian@unl.edu

https://doi.org/10.1021/acsami.4c12079
ACS Appl. Mater. Interfaces 2024, 16, 70763−70773

Ufuk Kilic − *Electrical and Computer Engineering Department, University of Nebraska-Lincoln, Lincoln, Nebraska 68588, United States*; Email: ufukkilic@unl.edu
Mohammad Ghashami − *Mechanical and Industrial Engineering Department, University of Illinois Chicago, Chicago, Illinois 60607, United States*; orcid.org/0000-0001-5033-0495; Email: ghashami@uic.edu

Authors

Sean L. Murray − *Mechanical and Materials Engineering Department, University of Nebraska-Lincoln, Lincoln, Nebraska 68588, United States*
Sahand Serajian − *Chemical and Biomolecular Engineering Department, University of Nebraska-Lincoln, Lincoln, Nebraska 68588, United States*; orcid.org/0000-0003-3667-2768
Syed Ibrahim Gnani Peer Mohamed − *Chemical and Biomolecular Engineering Department, University of Nebraska-Lincoln, Lincoln, Nebraska 68588, United States*
Shiseido Robinson − *Department of Industrial and Manufacturing Systems Engineering, Kansas State University, Manhattan, Kansas 66506, United States*
Rajavel Krishnamoorthy − *Department of Industrial and Manufacturing Systems Engineering, Kansas State University, Manhattan, Kansas 66506, United States*
Suprem R. Das − *Department of Industrial and Manufacturing Systems Engineering, Kansas State University, Manhattan, Kansas 66506, United States*; orcid.org/0000-0003-0334-7600
Siamak Nejati − *Chemical and Biomolecular Engineering Department, University of Nebraska-Lincoln, Lincoln, Nebraska 68588, United States*; orcid.org/0000-0002-1807-2796
Mathias Schubert − *Electrical and Computer Engineering Department, University of Nebraska-Lincoln, Lincoln, Nebraska 68588, United States*

Complete contact information is available at: https://pubs.acs.org/10.1021/acsami.4c12079

Author Contributions

#S.L.M. and S.S. contributed equally to this work. S.L.M. fabricated thin film samples and contributed to the introduction and methods sections; S.S. led the synthesis of Titanium Carbide MXene solution, fabricated thin films, and contributed to the introduction and methods sections; S.I.G.P.M. led topological characterization and contributed to the characterization and methods sections; S.R. led the synthesis of Titanium Carbide MXene solution for bulk-like films; R.K. conducted synthesis of Titanium Carbide MXene solution for bulk-like films; S.R.D. supervised thick MXene sample synthesis and fabrication and secured funding; M.B. supervised the project, contributed to the writing of the manuscript, and secured funding; S.N. supervised thin film synthesis, fabrication, and characterization and secured funding; U.K. secured funding, led the optical characterization of Titanium Carbide MXene, supervised the project, prepared the relevant figures, contributed to the writing of the characterization, optical response, and methods sections, and designed the TOC figure; M.S. contributed to the optical characterization and secured funding; M.G. supervised the project, secured funding, coordinated collaboration, and contributed to research conceptualization and manuscript writing. The manuscript was reviewed and approved by all authors.

Notes

The authors declare no competing financial interest.

■ ACKNOWLEDGMENTS

S.L.M. and M.G. acknowledge funding through the National Science Foundation (NSF) under grant No. OIA-2044049 and NASA Nebraska Space Grant Federal Award No. 80NSSC20M0112. U.K. and M.S. acknowledge the support provided by the NSF under awards ECCS 2329940, NSF-CMMI 2211858, NSF-DMR 2224456, and OIA-2044049 Emergent Quantum Materials and Technologies (EQUATE), by the Air Force Office of Scientific Research under awards FA9550-19-S-0003, FA9550-21-1-0259, and FA9550-23-1-0574 DEF, by the University of Nebraska Foundation, and the J. A. Woollam Foundation. S.R.D. acknowledges support from NSF Signals in the Soil (SitS) grant No. CBET 1935676.

■ REFERENCES

(1) Naguib, M.; Kurtoglu, M.; Presser, V.; Lu, J.; Niu, J.; Heon, M.; Hultman, L.; Gogotsi, Y.; Barsoum, M. W. Two-dimensional Nanocrystals Produced by Exfoliation of Ti3AlC2. *Adv. Mater.* **2011**, *23*, 4248−4253.
(2) Georgantas, Y.; Moissinac, F. P.; Bissett, M. MXenes-mining: A Decade of Discovery. *Graphene and 2D Materials* **2023**, 1−22.
(3) Shan, G.; Ding, Z.; Gogotsi, Y. Two-dimensional MXenes and their Applications. *Front. Phys.* **2023**, *18*, No. 13604.
(4) VahidMohammadi, A.; Rosen, J.; Gogotsi, Y. The World of Two-dimensional Carbides and Nitrides (MXenes). *Science* **2021**, *372*, No. eabf1581.
(5) Jiang, M.; Li, M.; Cui, C.; Wang, J.; Cheng, Y.; Wang, Y.; Zhang, X.; Qin, J.; Cao, M. Molecular-Level Interfacial Chemistry Regulation of MXene Enables Energy Storage beyond Theoretical Limit. *ACS Nano* **2024**, *18*, 7532−7545.
(6) Gogotsi, Y.; Huang, Q. MXenes: Two-dimensional Building Blocks for Future Materials and Devices. *ACS Nano* **2021**, *15*, 5775−5780.
(7) Anasori, B.; Naguib, M.; Editors, G. Two-dimensional MXenes. *MRS Bull.* **2023**, *48*, 238−244.
(8) Kurtoglu, M.; Naguib, M.; Gogotsi, Y.; Barsoum, M. W. First Principles Study of Two-dimensional Early Transition Metal Carbides. *MRS Commun.* **2012**, *2*, 133−137.
(9) Zhang, N.; Zhang, J.; Zhu, X.; Yuan, S.; Wang, D.; Xu, H.; Wang, Z. Synergistic Effect of Ti3C2Tx MXene Nanosheets and Tannic Acid-Fe3+ Network in Constructing High-Performance Hydrogel Composite Membrane for Photothermal Membrane Distillation. *Nano Lett.* **2024**, *24*, 724−732.
(10) Ronchi, R. M.; Arantes, J. T.; Santos, S. F. Synthesis, Structure, Properties and Applications of MXenes: Current Status and Perspectives. *Ceram. Int.* **2019**, *45*, 18167−18188.
(11) Zhang, D.; Shah, D.; Boltasseva, A.; Gogotsi, Y. MXenes for Photonics. *ACS Photonics* **2022**, *9*, 1108−1116.
(12) Liang, Q.; Wang, S.; Lu, X.; Jia, X.; Yang, J.; Liang, F.; Xie, Q.; Yang, C.; Qian, J.; Song, H.; Chen, R. High-Entropy MXene as Bifunctional Mediator toward Advanced Li-S Full Batteries. *ACS Nano* **2024**, *18*, 2395−2408.
(13) Li, P.; Wang, H.; Ju, Z.; Jin, Z.; Ma, J.; Yang, L.; Zhao, X.; Xu, H.; Liu, Y. Ti3C2Tx MXene-and Sulfuric Acid-Treated Double-Network Hydrogel with Ultralow Conductive Filler Content for Stretchable Electromagnetic Interference Shielding. *ACS Nano* **2024**, *18*, 2906−2916.
(14) Li, Y.; Yuan, Z.; Li, D.; Li, J.; Zhang, Y.; Wang, M.; Li, G.; Wang, L.; Han, W. Multi-interface Combination of Bimetallic Selenide and V4C3Tx MXene for High-Rate and Ultrastable Sodium Storage Devices. *ACS Nano* **2024**, *15*, 7439−7450.

(15) Chen, L.; Shi, X.; Yu, N.; Zhang, X.; Du, X.; Lin, J. Measurement and Analysis of Thermal Conductivity of Ti3C2Tx MXene Films. *Materials* **2018**, *11*, 1701.
(16) Wu, H.; Gu, J.; Li, Z.; Liu, W.; Bao, H.; Lin, H.; Yue, Y. Characterization of Phonon Thermal Transport of Ti3C2Tx MXene Thin Film. *J. Phys.: Condens. Matter* **2022**, *34*, No. 155704.
(17) Schultz, T.; Frey, N. C.; Hantanasirisakul, K.; Park, S.; May, S. J.; Shenoy, V. B.; Gogotsi, Y.; Koch, N. Surface Termination Dependent Work Function and Electronic Properties of Ti3C2Tx MXene. *Chem. Mater.* **2019**, *31*, 6590−6597.
(18) Kang, D. J.; Lee, K. H.; Noh, S. H.; Shin, H.; Jeong, W.; Lee, H.; Seo, Y.; Han, T. H. Impermeable Graphene Skin Increases the Heating Efficiency and Stability of an MXene Heating Element. *Small* **2023**, *19*, No. 2301077.
(19) Li, Y.; Xiong, C.; Huang, H.; Peng, X.; Mei, D.; Li, M.; Liu, G.; Wu, M.; Zhao, T.; Huang, B. 2D Ti3C2Tx MXenes: Visible Black but Infrared White Materials. *Adv. Mater.* **2021**, *33*, No. 2103054.
(20) Han, M.; Maleski, K.; Shuck, C. E.; Yang, Y.; Glazar, J. T.; Foucher, A. C.; Hantanasirisakul, K.; Sarycheva, A.; Frey, N. C.; May, S. J.; et al. Tailoring Electronic and Optical Properties of MXenes through Forming Solid Solutions. *J. Am. Chem. Soc.* **2020**, *142*, 19110−19118.
(21) Li, L.; Deng, Z.; Chen, M.; Yu, Z.-Z.; Russell, T. P.; Zhang, H.-B. 3D Printing of Ultralow-concentration 2D Nanomaterial Inks for Multifunctional Architectures. *Nano Lett.* **2023**, *23*, 155−162.
(22) Ontiveros, D.; Viñes, F.; Sousa, C. Bandgap Engineering of MXene Compounds for Water splitting. *J. Mater. Chem. A* **2023**, *11*, 13754−13764.
(23) Zhang, P.; Shou, H.; Xia, Y.; Wang, C.; Wei, S.; Xu, W.; Chen, Y.; Liu, Z.; Guo, X.; Zhu, K.; et al. X-ray Insights into Formation of- O Functional Groups on MXenes: Two-Step Dehydrogenation of Adsorbed Water. *Nano Lett.* **2023**, *23*, 1401−1408.
(24) Chaudhuri, K.; Alhabeb, M.; Wang, Z.; Shalaev, V. M.; Gogotsi, Y.; Boltasseva, A. Highly Broadband Absorber Using Plasmonic Titanium Carbide (MXene). *Acs Photonics* **2018**, *5*, 1115−1122.
(25) Lin, H.; Wang, X.; Yu, L.; Chen, Y.; Shi, J. Two-dimensional Ultrathin MXene Ceramic Nanosheets for Photothermal Conversion. *Nano Lett.* **2017**, *17*, 384−391.
(26) Mauchamp, V.; Bugnet, M.; Bellido, E. P.; Botton, G. A.; Moreau, P.; Magne, D.; Naguib, M.; Cabioc'h, T.; Barsoum, M. W. Enhanced and Tunable Surface Plasmons in Two-dimensional Ti_3C_2 Stacks: Electronic Structure Versus Boundary Effects. *Phys. Rev. B* **2014**, *89*, No. 235428.
(27) Dillon, A. D.; Ghidiu, M. J.; Krick, A. L.; Griggs, J.; May, S. J.; Gogotsi, Y.; Barsoum, M. W.; Fafarman, A. T. Highly Conductive Optical Quality Solution-processed Films of 2D Titanium Carbide. *Adv. Funct. Mater.* **2016**, *26*, 4162−4168.
(28) Panova, D. A.; Tselikov, G. I.; Ermolaev, G. A.; Syuy, A. V.; Zimbovskii, D. S.; Kapitanova, O. O.; Yakubovsky, D. I.; Mazitov, A. B.; Kruglov, I. A.; Vyshnevyy, A. A.; et al. Broadband Optical Properties of Ti3C2MXene Revisited. *Opt. Lett.* **2024**, *49*, 25−28.
(29) Zhang, Q.; Yan, L.; Yang, M.; Wu, G.; Hu, M.; Li, J.; Yuan, K.; Yang, X. Ultrafast Transient Spectra and Dynamics of MXene (Ti3C2Tx) in Response to Light Excitations of Various Wavelengths. *J. Phys. Chem. C* **2020**, *124*, 6441−6447.
(30) Lee, K.; Kwon, S.-y.; Woo, T.; Ryu, J.; Jung, J.; Lee, J. H. Nonlinear Absorption and Refraction Properties of V4C3MXene and its Use for an Ultra-Broadband Saturable Absorber. *Adv. Opt. Mater.* **2023**, No. 2300213.
(31) Liu, Y.; Xu, Y.; Xu, C.; Chen, J.; Liu, H.; Zhang, H.; Jin, L.; Fan, J.; Zou, Y.; Ma, X. Interface Charge Transfer in MXenes/Graphene Heterostructures for Ultrafast Photonics. *Adv. Opt. Mater.***2024***12*. 2301439..
(32) Han, M.; Yin, X.; Hantanasirisakul, K.; Li, X.; Iqbal, A.; Hatter, C. B.; Anasori, B.; Koo, C. M.; Torita, T.; Soda, Y.; et al. Anisotropic MXene Aerogels with a Mechanically Tunable Ratio of Electromagnetic Wave Reflection to Absorption. *Adv. Opt. Mater.* **2019**, *7*, No. 1900267.
(33) Xu, D.; Li, Z.; Li, L.; Wang, J. Insights into the Photothermal Conversion of 2D MXene Nanomaterials: Synthesis, Mechanism, and Applications. *Adv. Funct. Mater.* **2020**, *30*, No. 2000712.
(34) Gao, Y.; Lin, J.; Chen, X.; Tang, Z.; Qin, G.; Wang, G. Engineering 2D MXene and LDH into 3D Hollow Framework for Boosting Photothermal Energy Storage and Microwave Absorption. *Small* **2023**, *19*, No. 2303113.
(35) Guzelturk, B.; Kamysbayev, V.; Wang, D.; Hu, H.; Li, R.; King, S. B.; Reid, A. H.; Lin, M.-F.; Wang, X.; Walko, D. A.; et al. Understanding and Controlling Photothermal Responses in MXenes. *Nano Lett.* **2023**, *23*, 2677−2686.
(36) Bark, H.; Thangavel, G.; Liu, R. J.; Chua, D. H.; Lee, P. S. Effective Surface Modification of 2D MXene toward Thermal Energy Conversion and Management. *Small Methods* **2023**, *7*, No. 2300077.
(37) Wang, P.-L.; Mai, T.; Zhang, W.; Qi, M.-Y.; Chen, L.; Liu, Q.; Ma, M.-G. Robust and Multifunctional Ti3C2Tx/Modified Sawdust Composite Paper for Electromagnetic Interference Shielding and Wearable Thermal Management. *Small* **2024**, *20*, 2304914.
(38) Hemmat, Z.; Yasaei, P.; Schultz, J. F.; Hong, L.; Majidi, L.; Behranginia, A.; Verger, L.; Jiang, N.; Barsoum, M. W.; Klie, R. F.; Salehi-Khojin, A. Tuning Thermal Transport through Atomically Thin Ti3C2Tz MXene by Current Annealing in Vacuum. *Adv. Funct. Mater.* **2019**, *29*, No. 1805693.
(39) Limbu, T. B.; Chitara, B.; Garcia Cervantes, M. Y.; Zhou, Y.; Huang, S.; Tang, Y.; Yan, F. Unravelling the Thickness Dependence and Mechanism of Surface-enhanced Raman Scattering on Ti3C2TX MXene Nanosheets. *J. Phys. Chem. C* **2020**, *124*, 17772−17782.
(40) Fan, X.; Ding, Y.; Liu, Y.; Liang, J.; Chen, Y. Plasmonic Ti3C2Tx MXene Enables Highly Efficient Photothermal Conversion for Healable and Transparent Wearable Device. *ACS Nano* **2019**, *13*, 8124−8134.
(41) Li, L.; Shi, M.; Liu, X.; Jin, X.; Cao, Y.; Yang, Y.; Wang, W.; Wang, J. Ultrathin Titanium Carbide (MXene) Films for High-temperature Thermal Camouflage. *Adv. Funct. Mater.* **2021**, *31*, No. 2101381.
(42) Zhao, Y.; Deng, C.; Yan, B.; Yang, Q.; Gu, Y.; Guo, R.; Lan, J.; Chen, S. One-Step Method for Fabricating Janus Aramid Nanofiber/MXene Nanocomposite Films with Improved Joule Heating and Thermal Camouflage Properties. *ACS Appl. Mater. Interfaces* **2023**, *15*, 55150−55162.
(43) Han, M.; Zhang, D.; Singh, A.; Hryhorchuk, T.; Shuck, C. E.; Zhang, T.; Bi, L.; McBride, B.; Shenoy, V. B.; Gogotsi, Y. Versatility of Infrared Properties of MXenes. *Mater. Today* **2023**, *64*, 31−39.
(44) Shamsabadi, A. A.; Fang, H.; Zhang, D.; Thakur, A.; Chen, C. Y.; Zhang, A.; Wang, H.; Anasori, B.; Soroush, M.; Gogotsi, Y.; Fakhraai, Z. The Evolution of MXenes Conductivity and Optical Properties Upon Heating in Air. *Small Methods* **2023**, *7*, No. 2300568.
(45) Natu, V.; Benchakar, M.; Canaff, C.; Habrioux, A.; Celerier, S.; Barsoum, M. W. A Critical Analysis of the X-ray Photoelectron Spectra of Ti3C2Tz MXenes. *Matter* **2021**, *4*, 1224−1251.
(46) Anasori, B.; Gogotsi, Y.Introduction to 2D Transition Metal Carbides and Nitrides (MXenes). In *2D Metal Carbides and Nitrides (MXenes) Structure, Properties and Applications* 2019; pp 3−12.
(47) Azadi, S. K.; Zeynali, M.; Asgharizadeh, S.; Fooladloo, M. A. Investigation of the Optical and Electronic Properties of Functionalized Ti3C2Mxene with Halid Atoms using DFT Calculation. *Mater. Today Commun.* **2023**, *35*, No. 106136.
(48) Lashgari, H.; Abolhassani, M.; Boochani, A.; Elahi, S.; Khodadadi, J. Electronic and Optical Properties of 2D Graphene-like Compounds Titanium Carbides and Nitrides: DFT Calculations. *Solid State Commun.* **2014**, *195*, 61−69.
(49) Pacheco-Peña, V.; Hallam, T.; Healy, N. MXene Supported Surface Plasmons on Telecommunications Optical Fibers. *Light: Sci. Applications* **2022**, *11*, 22.
(50) Jeon, J.; Yang, Y.; Choi, H.; Park, J.-H.; Lee, B. H.; Lee, S. MXenes for Future Nanophotonic Device Applications. *Nanophotonics* **2020**, *9*, 1831−1853.

(51) Kim, H.; Wang, Z.; Alshareef, H. N. MXetronics: Electronic and Photonic Applications of MXenes. *Nano Energy* **2019**, *60*, 179−197.
(52) Chen, Z.; Sui, X.; Li, Y.; Liu, X.; Zhang, Y.; Ti3AlC2, M. A. X. Ti3AlC2MAX and Ti3C2MXene Quantum Sheets for Record-high Optical Nonlinearity. *J. Phys. Chem. Lett.* **2022**, *13*, 3929−3936.
(53) Sivasankarapillai, V. S.; Somakumar, A. K.; Joseph, J.; Nikazar, S.; Rahdar, A.; Kyzas, G. Z. Cancer Theranostic Applications of MXene Nanomaterials: Recent Updates. *Nano-Struct. Nano-Objects* **2020**, *22*, No. 100457.
(54) Tompkins, H. G.; Tasic, S.; Baker, J.; Convey, D. Spectroscopic Ellipsometry Measurements of Thin Metal Films. *Surface and Interface Analysis* **2000**, *29*, 179−187.
(55) Kılıç, U.; Sekora, D.; Mock, A.; Korlacki, R.; Valloppilly, S.; Echeverría, E. M.; Ianno, N.; Schubert, E.; Schubert, M. Critical-point Model Dielectric Function Analysis of WO3 Thin Films Deposited by Atomic Layer Deposition Techniques. *J. Appl. Phys.* **2018**, *124*, 11.
(56) Hilfiker, J. N.; Singh, N.; Tiwald, T.; Convey, D.; Smith, S. M.; Baker, J. H.; Tompkins, H. G. Survey of Methods to Characterize Thin Absorbing Films with Spectroscopic Ellipsometry. *Thin Solid Films* **2008**, *516*, 7979−7989.
(57) Kilic, U.; Mock, A.; Sekora, D.; Gilbert, S.; Valloppilly, S.; Melendez, G.; Ianno, N.; Langell, M.; Schubert, E.; Schubert, M. Precursor-surface Interactions Revealed during Plasma-enhanced Atomic Layer Deposition of Metal Oxide Thin Films by In-situ Spectroscopic Ellipsometry. *Sci. Rep.* **2020**, *10*, No. 10392.
(58) Järrendahl, K.; Arwin, H. Multiple Sample Analysis of Spectroscopic Ellipsometry Data of Semi-transparent Films. *Thin Solid Films* **1998**, *313−314*, 114−118.
(59) Heinemeyer, U.; Hinderhofer, A.; Alonso, M.; Ossó, J.; Garriga, M.; Kytka, M.; Gerlach, A.; Schreiber, F. Uniaxial Anisotropy of Organic Thin Films Determined by Ellipsometry. *Phys. Status Solidi A* **2008**, *205*, 927−930.
(60) Easwarakhanthan, T.; Beyssen, D.; Le Brizoual, L.; Alnot, P. Forouhi-Bloomer and Tauc-Lorentz Optical Dispersions Applied using Spectroscopic Ellipsometry to Plasma-deposited Fluorocarbon Films. *J. Appl. Phys.* **2007**, *101*, 7.
(61) Fujiwara, H. *Spectroscopic Ellipsometry: Principles and Applications*; John Wiley & Sons, 2007.
(62) Fang, S. J.; Chen, W.; Yamanaka, T.; Helms, C. Influence of Interface Roughness on Silicon Oxide Thickness Measured by Ellipsometry. *J. Electrochem. Soc.* **1997**, *144*, No. L231.
(63) Petrik, P.; Fried, M.; Lohner, T.; Berger, R.; Bıró, L.; Schneider, C.; Gyulai, J.; Ryssel, H. Comparative Study of Polysilicon-on-oxide using Spectroscopic Ellipsometry, Atomic Force Microscopy, and Transmission Electron Microscopy. *Thin Solid Films* **1998**, *313−314*, 259−263.
(64) Adachi, S.; Matsumura, T. M. T.; Suzuki, T. S. T. Optical Properties of Ion-Implanted Si Layeres Studied by Spectroscopic Ellipsometry. *Jpn. J. Appl. Phys.* **1994**, *33*, 1931.
(65) Synowicki, R. Spectroscopic Ellipsometry Characterization of Indium Tin Oxide Film Microstructure and Optical Constants. *Thin Solid Films* **1998**, *313−314*, 394−397.
(66) Chen, S.; Kühne, P.; Stanishev, V.; Knight, S.; Brooke, R.; Petsagkourakis, I.; Crispin, X.; Schubert, M.; Darakchieva, V.; Jonsson, M. P. On the Anomalous Optical Conductivity Dispersion of Electrically Conducting Polymers: Ultra-wide Spectral Range Ellipsometry Combined with a Drude-Lorentz Model. *J. Mater. Chem. C* **2019**, *7*, 4350−4362.
(67) Hwang, J.; Schwendeman, I.; Ihas, B.; Clark, R.; Cornick, M.; Nikolou, M.; Argun, A.; Reynolds, J.; Tanner, D. In Situ Measurements of the Optical Absorption of Dioxythiophene-based Conjugated Polymers. *Phys. Rev. B* **2011**, *83*, No. 195121.
(68) Tiwald, T. E.; Thompson, D. W.; Woollam, J. A.; Paulson, W.; Hance, R. Application of IR Variable Angle Spectroscopic Ellipsometry to the Determination of Free Carrier Concentration Depth Profiles. *Thin Solid Films* **1998**, *313−314*, 661−666.
(69) De Sousa Meneses, D.; Malki, M.; Echegut, P. Structure and Lattice Dynamics of Binary Lead Silicate Glasses Investigated by Infrared Spectroscopy. *J. Non-Cryst. Solids* **2006**, *352*, 769−776.
(70) Ashcroft, N.; Mermin, N. *Solid State Physics, Holt*; Rinehart and Winston: New York, 1976, *2005*, p. 403.

https://doi.org/10.1021/acsami.4c12079
ACS Appl. Mater. Interfaces 2024, 16, 70763−70773